nature biotechnology

A FRET sensor enables quantitative measurements of membrane charges in live cells

Yuanqing Ma[1,2], Yui Yamamoto[1,2], Philip R Nicovich[1,2], Jesse Goyette[1,2], Jérémie Rossy[1], J Justin Gooding[3,4] & Katharina Gaus[1,2]

Membrane charge has a critical role in protein trafficking and signaling. However, quantification of the effective electrostatic potential of cellular membranes has remained challenging. We developed a fluorescence membrane charge sensor (MCS) that reports changes in the membrane charge of live cells via Förster resonance energy transfer (FRET). MCS is permanently attached to the inner leaflet of the plasma membrane and shows a linear, reversible and fast response to changes of the electrostatic potential. The sensor can monitor a wide range of cellular treatments that alter the electrostatic potential, such as incorporation and redistribution of charged lipids and alterations in cytosolic ion concentration. Applying the sensor to T cell biology, we used it to identify charged membrane domains in the immunological synapse. Further, we found that electrostatic interactions prevented spontaneous phosphorylation of the T cell receptor and contributed to the formation of signaling clusters in T cells.

Many cellular processes, including endocytosis, exocytosis and signaling, are regulated by the reversible association of proteins with the plasma membrane[1–3]. Typically, protein-membrane associations are controlled by both hydrophobic and electrostatic interactions. Hydrophobic interactions include the insertion of aromatic amino acid into the hydrophobic core of the lipid bilayer[4] and lipid modifications of the protein such as palmitoylation, myristoylation and farnesylation[5]. Unlike many hydrophobic interactions, electrostatic protein-membrane interactions are often highly reversible. Negatively charged phospholipids generate an electric potential at the inner surface of membrane that attracts cations and proteins with polybasic motifs.

There are many examples of electrostatic interactions between proteins and the cytosolic face of the plasma membrane influencing membrane targeting, protein conformation and activity. For example, changes in phosphatidylinositol (PI) phosphorylation levels change membrane charge and regulate phagocytosis[2], electrostatic interactions between syntaxin-1A and negatively charged phosphatidylinositol biphosphate (PIP_2) domains modulate neurotransmitter release at neuronal synapses[6], and the rate of ionic exchange by the Na^+/H^+ exchanger NHE3 is controlled by electrostatic interaction between its cytoplasmic tail and acidic phospholipids[7]. Similarly, electrostatic interactions have also been implicated in regulating the kinase activity of the epidermal growth factor receptor (EGFR)[1].

Monovalent and polyvalent anionic phospholipids at the inner leaflet of plasma membrane create a negative potential[8] of ~−30 mV that is independent of the transmembrane potential[3,9]. Although there are many fluorescence reporters that respond to changes in transmembrane potential, there is only one reporter that senses the electrostatic potential of cellular membranes. Okeley and Gelb[10] and colleagues of Grinstein[2] pioneered the development of a sensor called R-pre that contains the membrane-localization motif of K-Ras, including a farnesylation site and polycationic amino acid sequence that electrostatically interacts with the plasma membrane[2]. When the negative electrostatic potential of the plasma membrane decreases, R-pre detaches from the inner leaflet of the plasma membrane[2]. Despite differences in plasma membrane lipid compositions, this sensor has been successfully used in a variety of cell types[2,7,11]. Alternatives to R-pre include fluorescent reporters that specifically interact with a particular lipid species, such as a fusion protein that contains the C2 domain of lactadherin, called Lact-C2, which detects phosphatidylserine (PS)[12]. As with R-pre, changes in the cellular distribution of the fluorescence intensity of the sensor are used as the read-out.

However, intensity-based measurements have limitations. First, the measurement is dependent on the local concentration of the sensor, which means that membrane ruffling and expression levels could influence the results. Furthermore, cell-to-cell comparisons are difficult, and quantification of membrane charges is challenging. For example, imaging methods with limited optical sectioning may not be able to reliably distinguish sensors bound to the plasma membrane from sensors in the cytoplasm. Finally, intensity-based measurements make it difficult to detect charged membrane domains in the plasma membrane. All of these limitations could be overcome with a FRET sensor that stably associates with the cytoplasmic leaflet of the plasma membrane.

We used R-pre to create a FRET-based sensor in which the decrease in electrostatic membrane interaction directly reduces the efficiency of energy transfer between donor and acceptor molecules on the same molecule. Because the number of donor and acceptor molecules is identical in each pixel, ratiometric measurements cancel out any variations in

[1]EMBL Australia Node in Single Molecule Science, School of Medical Sciences, University of New South Wales, Sydney, New South Wales, Australia. [2]ARC Centre of Excellence in Advanced Molecular Imaging, University of New South Wales, Sydney, New South Wales, Australia. [3]School of Chemistry and Australian Centre of NanoMedicine, University of New South Wales, Sydney, New South Wales, Australia. [4]ARC Centre of Excellence in Convergent Bio-Nano Science and Technology, University of New South Wales, Sydney, New South Wales, Australia. Correspondence should be addressed to K.G. (k.gaus@unsw.edu.au).

Received 15 September 2015; accepted 15 February 2017; published online 13 March 2017; corrected after print 30 March 2017; doi:10.1038/nbt.3828

sensor concentrations. In addition, our MCS is permanently attached to the plasma membrane by hydrophobic interactions, which reduces the signals from the cytoplasm and provides an improved signal-to-noise ratio. Unlike R-pre, MCS responses were reversible and enabled fast spatial and temporal mapping of the effective electrostatic potential at the single-cell level and across the cell surface. We examined the effect of calcium influx, hypo- and hypertonic treatments, PS levels, and changes in PI phosphorylation on electrostatic membrane interactions and detected distinct charged membrane domains in the immunological synapse.

RESULTS

Design of the FRET-based MCS

The sensor consists of two membrane attachment units (MA1 and MA2) on either side of two fluorescent proteins (FP1 and FP2) that are connected with a short linker (**Fig. 1a**). The first unit is a permanent, hydrophobic membrane anchor that stably attaches the sensor to the plasma membrane and consists of either a myristoylation and two palmitoylation groups (Lck10; **Fig. 1b**,**c**) or a myristoylation group and a stretch of positively charged residues (Src15; **Fig. 1c**). The second membrane attachment unit (**Fig. 1a**) is an electrostatic anchor, comprising the original or modified versions of R-pre (**Fig. 1c**)[2]. When the membrane potential is highly negative, the dipoles of two fluorescent proteins are aligned, which should result in high FRET efficiency. When the membrane charge is reduced, MA2 with the R-Pre unit detaches from the plasma membrane, whereas the MA1 subunit retains the sensor on the membrane. However, MA2 detachment should cause a change in the dipole alignment of the two fluorophores and hence a reduced FRET efficiency (**Fig. 1a**).

The effective electrostatic potential at an interface is governed by the surface charge density and concentration of counter ions in the solution[8,9,13,14]. In the context of the cell membrane, the negatively charged lipids in the plasma membrane create an electrostatic field in the adjacent intracellular space. Positively charged ions such as K^+ and Na^+ are attracted to the charged surface and form a layer of positively charged ions. As a result, the apparent membrane electrostatic charge is substantially reduced as a result of this ion shielding effect. The apparent electrostatic charge is reflected in the zeta potential whose spatial distribution is described by the Gouy-Chapman-Stern theory of the electrical double bilayer. Accordingly, the Debye length[8], which is inversely proportional to the square root of the ionic strength of the solution, quantifies the net electrostatic effect of the charged surface onto molecules in solution. It is ~0.9 nm in 10 mM NaCl, ~0.3 nm in 100 mM NaCl solution and ~0.2 nm at the ionic strength of the cytoplasm[15]. Given these Debye lengths, it is essential that the sensor is located in close proximity to the membrane under a wide range of conditions and is permanently anchored to the membrane.

To optimize the MCS, we aligned the two fluorescent proteins to achieve high FRET efficiency when membrane potential was highly negative (Online Methods and **Supplementary Fig. 1a–c**). We also modified R-pre to retain the sensor at the plasma membrane even at low negative electrostatic potentials (**Supplementary Figs. 1d**,**e** and **2**). Next, we tuned the binding efficiency of the electrostatic anchor to the inner leaflet of the plasma membrane to arrive at two versions of the sensor: MCS and MCS^+ (**Fig. 1c**). We also engineered controls constructs in which the charge-sensitive arm MA2 was replaced with hydrophobic membrane attachment motif of H-Ras (MCS Hras; **Fig. 1c**), which was largely charge insensitive after further modifications (MCS Hras FI; **Fig. 1c**,**d**).

Characterization of MCS FRET responses

To characterize the performance of the sensors, we titrated the ionic strength of the solution and thereby altered the zeta potential of the

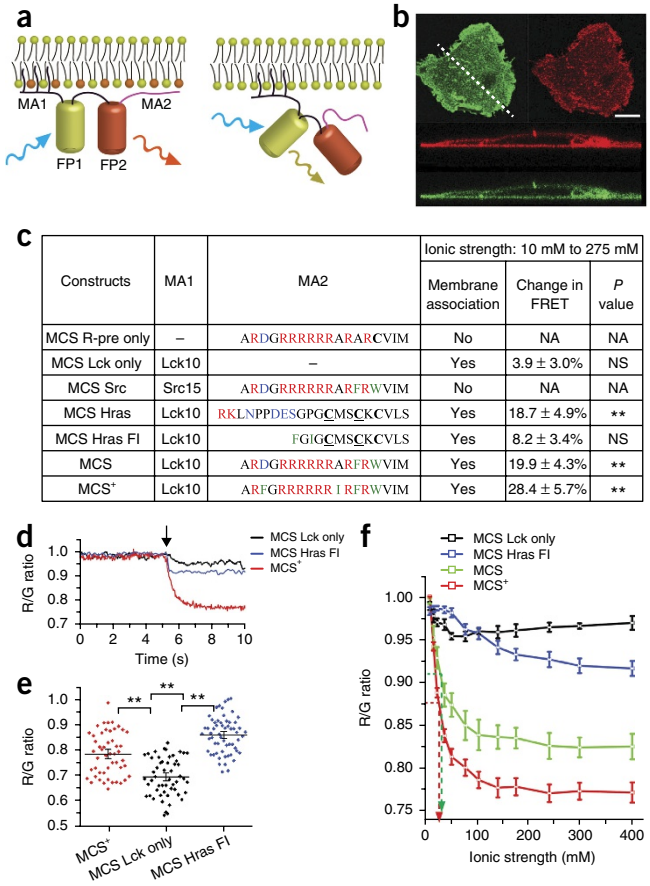

Figure 1 MCS and MCS^+ are FRET-based sensors that report the effective electrostatic potential of the plasma membrane. (**a**) The charge sensor consists of two membrane attachment (MA) units and two fluorescent proteins (FP) separated by a short linker. MA1 is a hydrophobic anchor containing a palmitoylation and myristoylation group that permanently associates with the membrane. MA2 (pink) is an electrostatic anchor that associates with the inner surface of the plasma membrane in a charge-dependent manner. When MA2 is attached to the membrane, the FRET efficiency is high; when MA2 is detached from the membrane, the FRET efficiency is low. (**b**) The MCS localized to the plasma membrane. Images of donor (green) and acceptor (red) fluorescence of MCS in a COS-7 cell in the *x-y* and *x-z* planes are shown. Images are representatives of $n = 10$ independent experiments. Scale bar represents 5 µm. (**c**) MA1 and MA2 in different versions of MCS. MCS Src has a myristoylation group and a stretch of positively charged residues as MA1. In the one letter amino acid codes of MA2, negatively charged amino acids are written in blue font, positively charged amino acids in red, hydrophobic residues in green, and farnesylated and palmitoylated residues are marked with **C** and **C**, respectively. Membrane association and change in FRET efficiency in membrane sheets in response to change in ionic strength from 10 mM to 275 mM are shown. Data are presented as mean and s.e. of $n = 7–10$ independent measurement; NA, not applicable; NS, not significant ($P > 0.05$), $^{**}P < 0.001$ (unpaired, two-tailed *t* test) compared with solution exchange at constant ionic strength (10 mM to 10 mM, change in FRET 7.5 ± 1.0%). (**d**,**e**) Change in normalized FRET efficiency (R/G ratio) in membrane sheets of MCS Lck only, MCS Hras FI and MCS^+ when ionic strength was changed from 10 mM to 275 mM (**d**), and the average FRET efficiencies in transfected COS-7 cells (**e**). Each symbol in **e** represents a FRET measurement in a single cell ($n = 30$; $^{**}P < 0.01$, one-way ANOVA test with Bonferroni *post hoc* test). (**f**) Ionic strength titration. Maximum normalized FRET efficiency (R/G ratio) of MCS^+ (red), MCS (green), MCS Lck only (black) and MCS Hras FI (blue) in membrane sheets in response to in ionic strength is shown. A 50% change in the R/G ratio (black arrow) estimated the membrane binding affinity ($K_d = 31 \pm 9$ mM for MCS and MCS^+; no significant difference). Data are presented as mean and s.e. of $n = 10$ independent experiments.

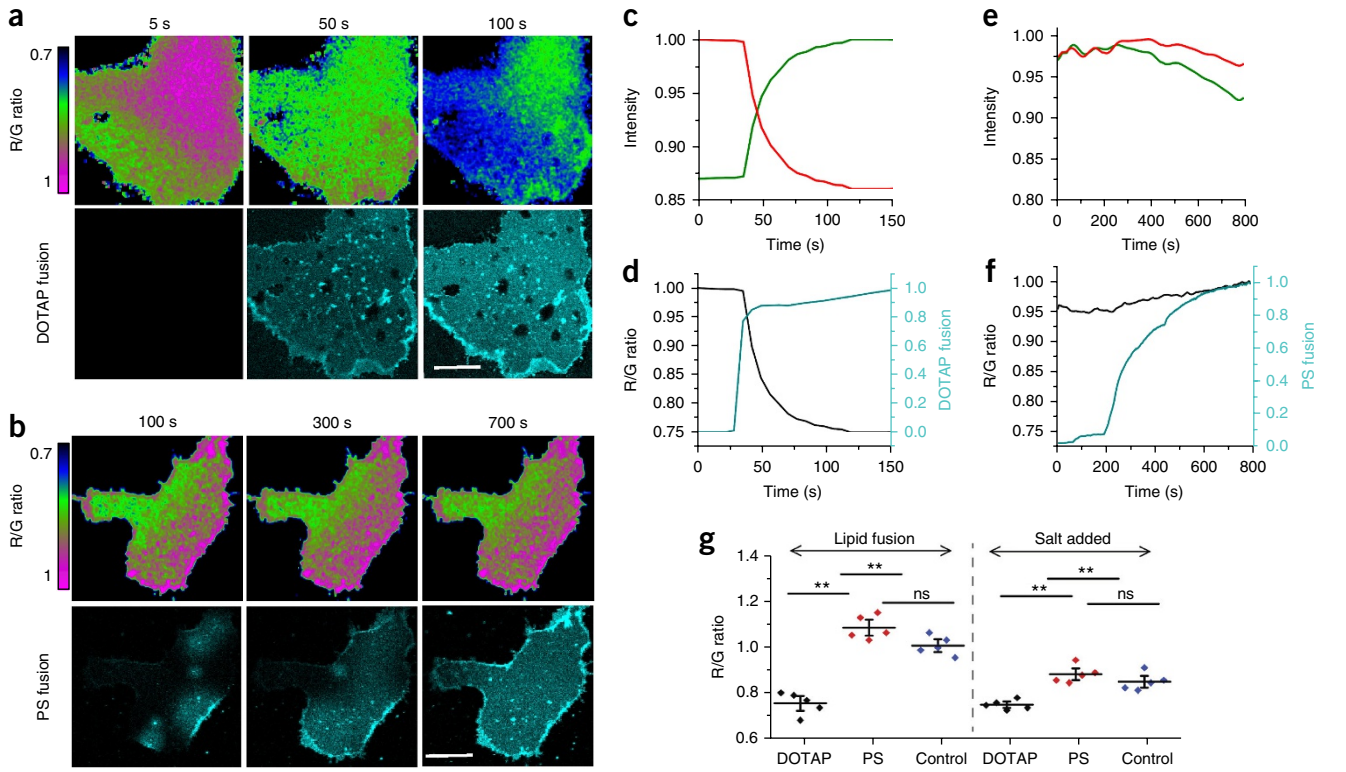

Figure 2 MCS$^+$ is sensitive to charged lipids in the plasma membrane. (**a**,**b**) Ratiometric FRET images (R/G ratio) of MCS$^+$ in membrane sheets during lipid vesicle fusion loaded with positively charged DOTAP (**a**) or negatively charged PS (**b**). Lipid fusion was monitored by the incorporation of fluorescent lipid DiR (cyan). R/G ratio images are pseudo-colored, as indicated. Scale bars represent 10 µm. (**c**–**f**) Change in donor (green, **c**,**e**) and acceptor (red, **c**,**e**) intensity, FRET efficiency (R/G ratio, black, **d**,**f**), and lipid incorporation (cyan, **d**,**f**) of MCS$^+$ after lipid vesicle fusion containing DOTAP (**c**,**d**) and PS (**e**,**f**). In **a**–**f**, images and data are representative of $n = 5$ independent experiments. (**g**) FRET efficiency (R/G ratio) of MCS$^+$ following lipid fusion (lipid fusion) and subsequent solution exchange from 10 mM to 275 mM on the same lipid-treated membrane sheet (salt added). Control treatments were lipid fusion vesicles that were not enriched in DOTAP or PS. Data are normalized to the mean of control membranes after lipid fusion. Data are presented as mean and s.e.m. of $n = 5$ independent experiments; ns, not significant ($P > 0.05$); $^{**}P < 0.01$ (one-way ANOVA with Bonferroni *post hoc* test).

membrane. To do so, we expressed the sensor in COS-7 cells and 'unroofed' cells as previously described[16]. This procedure leaves an exposed membrane sheet on the glass coverslips on which the cells were originally seeded with the inner plasma membrane facing the solution. We either introduced a step-change in the ionic strength from 10 mM to 275 mM (**Fig. 1d**) or gradually increased the ionic strength from 10 mM to 400 mM (**Fig. 1f**) using buffers that contained no Ca^{2+} and Mg^{2+} ions. We measured FRET efficiency as the ratio of acceptor to donor fluorescence and performed control experiments to verify the imaging conditions (**Supplementary Figs. 3**–**5**). Although loss of focus as a result of solution exchange could only account for a change in FRET efficiency of 7.5 ± 1.0% (**Fig. 1c** and **Supplementary Fig. 5**), MCS and MCS$^+$ had a maximum FRET range of 19.9 ± 4.3% and 28.4 ± 5.7%, respectively (**Fig. 1c**). Furthermore, both MCS and MCS$^+$ responded to ionic strength in the physiological relevant window of <150 mM and had K_d values of 31 ± 9 mM (**Fig. 1f**).

In contrast with MCS and MCS$^+$, the control constructs MCS Lck only and MCS Hras FI exhibited different FRET efficiencies in intact cells (**Fig. 1e**) and no significant change in FRET efficiency in response to ionic strength (**Fig. 1c**,**d**,**f**), indicating that membrane detachment of MA2 was the charge-sensitive element in MCS and MCS$^+$ as per design. The original R-pre construct[2] and the MCS R-pre only construct (**Fig. 1c**) detached from the plasma membrane (**Supplementary Fig. 6a**–**d**), making precise quantification of their responses difficult.

A further confirmation that the FRET signal represents the overall zeta potential of the membrane came from fitting the FRET efficiency to the Debye-Hückel model (**Supplementary Fig. 7**). We made the assumption that the sensor exists in two discrete states: with the electrostatic membrane anchor attached or not attached to the cell membrane. The excellent agreement of the experimental data with the model for both MCS and MCS$^+$ demonstrated that a linear relationship exists between the FRET value and the effective electrostatic potential of the membrane.

A notable characteristic of MCS is that its response was reversible (**Supplementary Fig. 8**). This allowed us to assess the timescale on which the sensor reacted to changes in membrane charge after rapid solution exchange. We first measured the membrane residence time, that is, the time it took to reach 50% change in FRET efficiency after the solution change and then calculated the values of the rate constants k_{on} and k_{off} from these membrane residence times. The sensor reacted rapidly (**Supplementary Fig. 8a**,**b**), with a k_{off} rate of ~12 s^{-1} (**Supplementary Fig. 8c**,**d**) and k_{on} rate of ~0.5 s^{-1} (**Supplementary Fig. 8e**), indicating that the sensor was fully reversible.

Instead of varying the concentration of counter ions in the solution, the effective electrostatic potential of a membrane can also be altered by modulating the charge density of the membrane[8,9,13], for example, by adding charged lipids. To do so, we fused lipid vesicles comprising the cationic lipid 1, 2-dioleoyloxy-3-trimethylammonium propane (DOTAP; **Fig. 2a**) and the anionic phospholipid PS (**Fig. 2b**) with membrane sheets containing MCS$^+$. DOTAP vesicle fusion, monitored via incorporation of a far-red fluorescent dye, rapidly altered the emission profile and FRET efficiency of MCS$^+$ (**Fig. 2c**,**d**), indicating

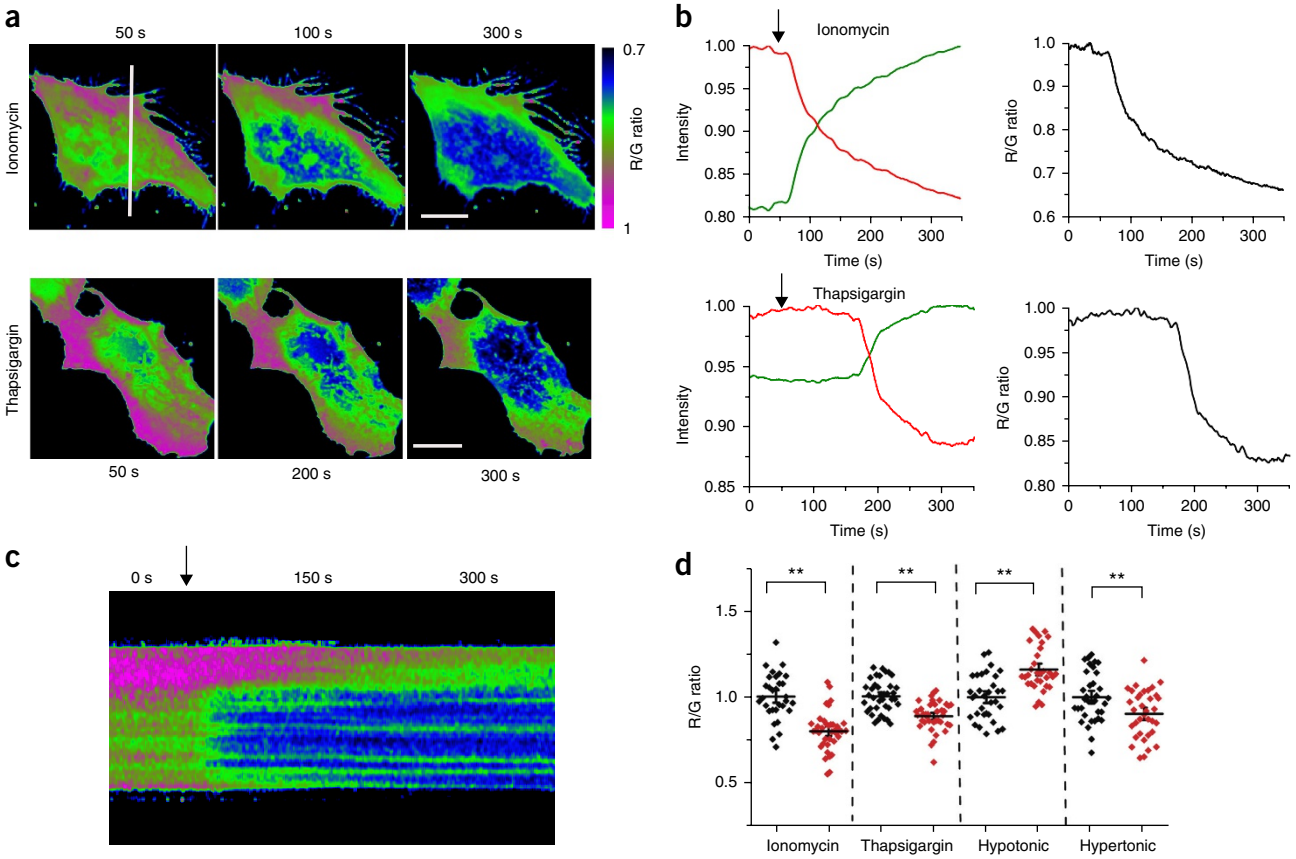

Figure 3 Intra- and extracellular ion concentrations affect the membrane charges at the inner leaflet of the plasma membrane. (**a**) Ratiometric FRET images (R/G ratio, pseud-colored as indicated by the color scale) of MCS$^+$ in live COS-7 cells during Ca^{2+} influx induced by ionomycin (10 μM) and thapsigargin (20 μM) treatment. Scale bars represent 10 μm. (**b**) Change in in donor (green) and acceptor (red) intensity and FRET efficiency (R/G ratio, black) for the ionomycin-and thapsigargin-treated cells shown in **a**. Arrows indicate when drugs were added. Images and data in **a** and **b** are representative of $n = 7$ independent experiments per condition. (**c**) Kymograph of R/G ratio across the plasma membrane at the position of the white line shown in **a**. (**d**) FRET efficiency of MCS$^+$ in COS-7 cells before (black symbols) and after (red symbols) ionomycin, thapsigargin, hypotonic (150 mM to 40 mM) and hypertonic (150 mM to 450 mM) treatments. FRET efficiencies were normalized to the mean of untreated cells. Each symbol is one measurement in one cell; horizontal and vertical bars represent mean and s.e.m., respectively. $^{**}P < 0.01$ (unpaired, two-tailed t test).

that changes in FRET were caused by the repulsion between the positively charged residues in MA2 and the positively charged lipids. As with increasing ionic strength, the MCS R-Pre only sensor detached from the membrane in response to the incorporation of cationic lipid DOTAP (**Supplementary Fig. 6c**). In contrast with DOTAP enrichment, incorporation of PS caused a small, but not statistically significant, increase in FRET efficiency of MCS$^+$ (**Fig. 2e**,**f**). To illustrate that the sensor had indeed responded to the effective electrostatic potential, we changed the ionic strength from 10 mM to 275 mM after lipid vesicle fusion (**Fig. 2g**). This caused only a 3 ± 2% change in FRET efficiency in DOTAP-enriched membrane sheets, strongly suggesting that the cationic lipids had already lowered the effective electrostatic potential, whereas the FRET efficiency exhibited the maximum change of 25 ± 5% in PS-enriched membrane sheets. We therefore concluded that the sensor faithfully responded to changes in the effective electrostatic potential irrespective of whether the changes were caused by the charge concentration in the membrane or the concentration of counter ions.

Performance of the MCS and MCS$^+$ in cells

We next tested the performance of the sensor in live and fixed cells. As in the membrane sheets, the effective electrostatic potential at cytoplasmic side of the plasma membrane can be reduced through ions in the cytoplasm (**Fig. 3**) or by reducing the density of negatively charged lipids in the inner leaflet (**Fig. 4**). In live cell imaging, it is advantageous that the sensor does not need to translocate from the membrane to report on the effective electrostatic potential. Combined with the fast response kinetics, the sensor was, for example, able to monitor the effect of calcium fluxes, induced with ionomycin or thapsigargin, on the capacity for electrostatic membrane interactions over time (**Fig. 3a**,**b**), the temporal evolution of the electrostatic potential across different regions of the plasma membrane (**Fig. 3c**) or at the endoplasmic reticulum (**Supplementary Fig. 9**). The consistent change in FRET efficiency reported by MCS$^+$ (**Fig. 3d**) was not observed for MCS Lck only and MCS Hras FI in response to thapsigargin treatment (**Supplementary Fig. 10**).

Treatment of cells with hypotonic solution results in the influx of water molecules, thereby reducing the concentration of ions in the cytoplasm and limiting the shielding effect of membrane charge. As expected from the ionic strength titration experiments, MCS$^+$ (**Fig. 3d**), but not MCS Lck only and MCS Hras FI (**Supplementary Fig. 10**), responded to hypotonic treatment with significantly enhanced FRET efficiency ($P < 0.01$; **Fig. 3d**), suggesting that the physiological ionic strength of the cytoplasm is sufficiently high to reduce the electrostatic interaction between the sensor and cellular membranes. Hypertonic treatments, on the other hand, cause an increase in intracellular

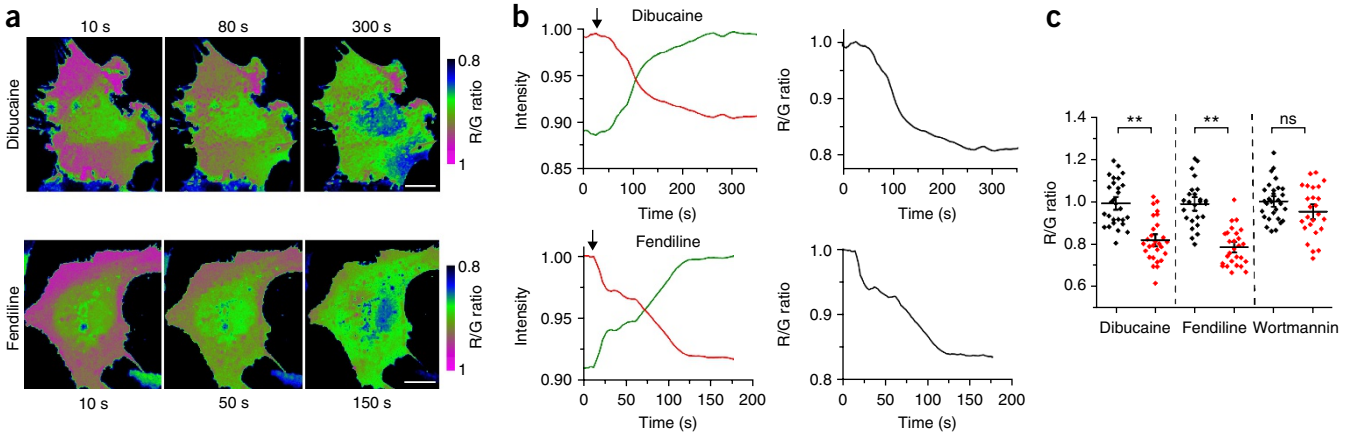

Figure 4 PS, but not PI, phosphorylation levels contribute to the effective electrostatic potential of the plasma membrane. Live Cos-7 cells expressing MCS$^+$ were treated with dibucaine (1 mM) to induce the flipping of PS from in the inner to the leaflet of the plasma membrane or with fendiline (60 μM) to cause PS redistribution from the plasma membrane to the cytosol. (**a**) Ratiometric FRET images (R/G ratio, pseud-colored as indicated by the color scale) of MCS$^+$ during dibucaine and fendiline treatment. Scale bars represent 5 μm. (**b**) Change in in donor (green) and acceptor (red) intensity and FRET efficiency (R/G ratio, black) for the dibucaine-and fendiline-treated cells shown in **a**. Arrows indicate when drugs were added. Images and data in **a** and **b** are representative of $n = 10$ independent experiments per condition. (**c**) FRET efficiency of MCS$^+$ in COS-7 cells before (black symbols) and after (red symbols) dibucaine, fendiline and wortmannin treatments in fixed cells. FRET efficiencies were normalized to the mean of untreated cells. Each symbol is one cell of $n = 30$ independent measurements; horizontal and vertical bars represent mean and s.e.m., respectively. ns, not significant ($P > 0.05$); $^{**}P < 0.01$ (unpaired, two-tailed t test).

cations[17,18] and reduce the effective electrostatic potential of the inner plasma membrane. We observed a reduced FRET efficiency for MCS$^+$ in response to hypertonic treatment (**Fig. 3d**), whereas the FRET efficiency increased for MCS Lck only and MCS Hras FI (**Supplementary Fig. 10**). Notably, the kinetics of the effective electrostatic potential in response to hypotonic and hypertonic treatments was markedly different (**Supplementary Fig. 11**), suggesting that the sensor could also be used to monitor the compensatory effects of membrane channels and pumps to these treatments.

Instead of altering the ionic strength of the cytoplasm, we also directly manipulated the membrane charge by flipping PS from the inner to the outer leaflet with the drug dibucaine or causing the relocation of PS from the plasma membrane to the cytosol with the drug fendiline (**Fig. 4a**). Both treatments resulted in a reduction in FRET efficiency of 22 ± 5% and 26 ± 7%, respectively (**Fig. 4a–c**), whereas MCS Lck only and MCS Hras FI were unresponsive to fendiline treatment (**Supplementary Fig. 12**). The sensitivity of MCS$^+$ to PS levels in the plasma membrane was expected, as PS is the most abundant negatively charged lipid in the inner leaflet of the plasma membrane. By contrast, acute changes in PI phosphorylation, as modulated by the inhibition of phosphoinositide 3-kinases with wortmannin (**Fig. 4c**), and inhibition of phosphatidylinositol-3,4,5-trisphosphate 3-phosphatase with bpV(HOpic) and bpV(phen) (data not shown) had no significant effects ($P > 0.05$; **Fig. 4c**) on the overall effective electrostatic potential as sensed by MCS$^+$. Chronic alteration of PI phosphorylation as achieved by overexpressing a 5′-specific phosphatidylinositol 4,5-bisphosphate phosphatase, Inp54p, resulted, however, in a significant reduction in FRET efficiency ($P < 0.01$; **Supplementary Fig. 13**), suggesting that the effective electrostatic potential can adapt to cellular conditions.

Finally, we benchmarked MCS$^+$ against the intensity-based sensors R-pre, Lact-C2 and Akt PH, all fused to GFP, by measuring the intensity ratio at the plasma membrane versus the cytoplasm in response to drug treatments (**Supplementary Fig. 14**). Similar to MCS and MCS$^+$, R-pre responded strongly to treatments with ionomycin, dibucaine and fendiline, whereas Lact-C2 only exhibited a strong response to ionomycin and fendiline. R-pre and Akt PH responses to wortmannin treatment were inconclusive as a result of large cell-to-cell variation. Even with an automated image analysis tool, the intensity-based sensors exhibited large standard errors, highlighting the advantage of a FRET-based probe for quantification.

Membrane charges at the T cell immunological synapse

Membrane charge is thought to be critical for T cell receptor (TCR) signaling. In resting cells, basic-rich stretch (BRS) motifs in the intracellular domains of the TCR-CD3 complex bind to negatively charged lipids in the cytoplasmic leaflet of the plasma membrane[11,19,20]. This interaction is thought to prevent spontaneous TCR signaling in resting T cells[21], although this has not been directly proven. During the process of TCR triggering, the cytoplasmic tails of the CD3 chains dissociate from the membrane through an as yet unknown mechanism, which affects both the phosphorylation and the mobility of the TCR-CD3 complex[19,20,22]. TCR triggering is associated with a decrease in intensity of fluorescently tagged R-pre and Lact-C2 sensors at the immunological synapse, indicating decreased charge and PS levels[11]. However, an earlier biochemical analysis of lipids at the immunological synapse demonstrated a clear increase in PS species[23], leaving open the possibility that changes in membrane ruffling, rather than differences in charge, influence the biochemical and/or the fluorescence intensity measurements. Thus, we reexamined charged membrane domains in the immunological synapse with our FRET-based charge sensor.

We expressed MCS$^+$ in the human T lymphocyte cell line Jurkat E6-1 and measured the change in membrane charge when cells were activated with either beads (**Supplementary Fig. 15**) or surfaces (**Fig. 5**) coated with anti-CD3 and anti-CD28 antibodies. We confirmed that the inner plasma membrane leaflet exhibited lower FRET efficiency and thus less negatively charged membranes at the T cell activation zone compared with regions of the membrane in which the TCR was not activated (**Supplementary Fig. 15**)[11].

Planar views of the immunological synapse revealed further details of the distribution of the electrostatic potential (**Fig. 5**). Using a custom-written algorithm to identify the center and periphery of the synapse, we found differences in effective electrostatic potential across

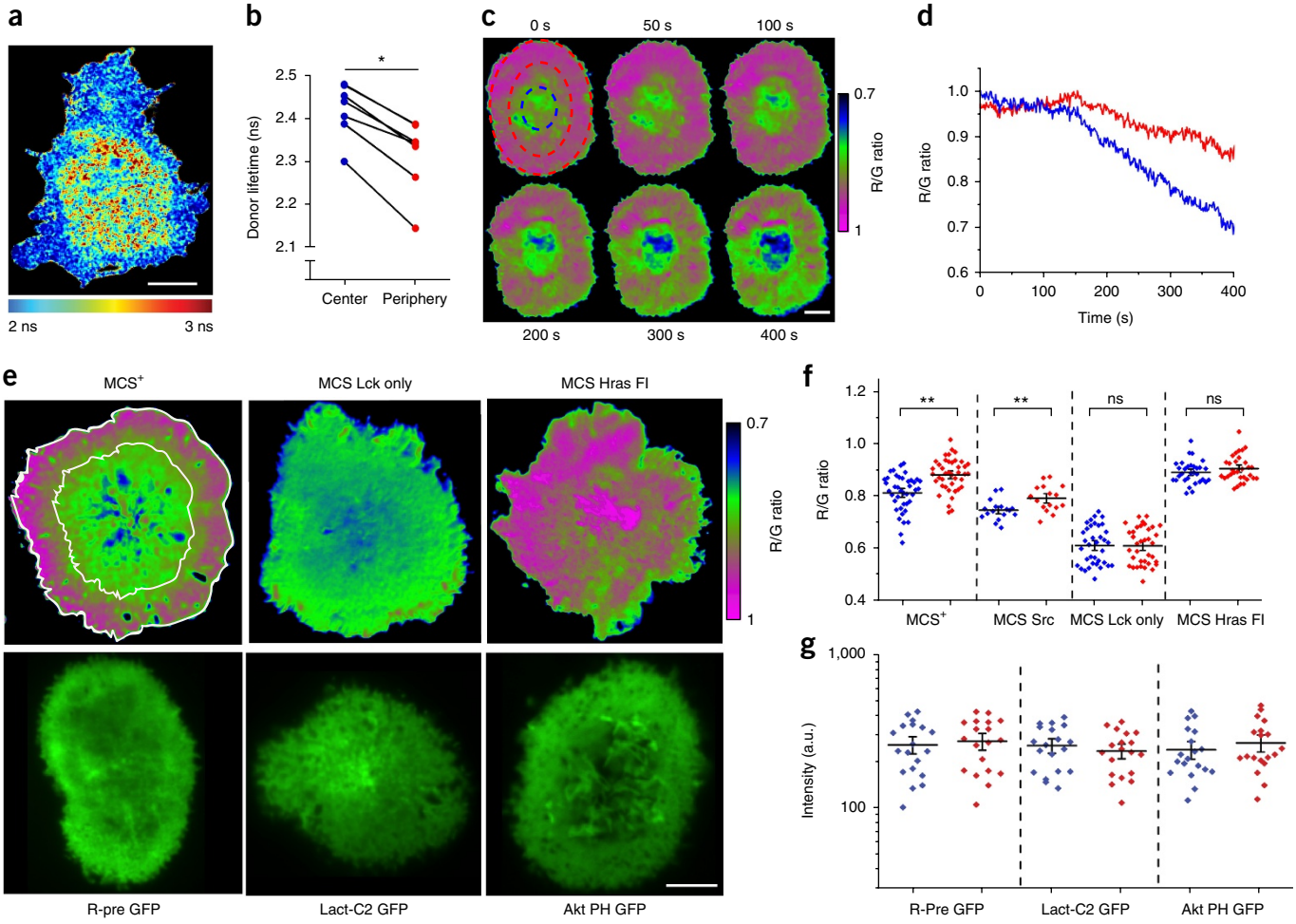

Figure 5 Membrane charge at the immunological synapse. Jurkat T cells were activated on coverslips coated with anti-CD3 and anti-CD28 antibodies and imaged at the glass-cell interface with fluorescence-lifetime imaging microscopy (FLIM, **a**,**b**) and total internal reflection fluorescence microscopy (TIRFM, **c**–**g**). (**a**,**b**) FLIM image (**a**, >200 photons per pixel) and values (**b**) of MCS$^+$ in activated Jurkat cells. Fluorescence donor lifetimes were pseudo-colored with blue to red reflecting short to long lifetimes or high to low FRET efficiencies. Regions corresponding to the central synapse (blue region and symbols) and peripheral synapse (red region and symbols) were identified with a custom-written algorithm that defined the periphery as the outer 30 pixels (~3 µm) of the intensity-thresholded synapse and remaining area as the center (as shown in **e**). In **b**, $*P < 0.05$ (paired t test, $n = 5$). (**c**,**d**) Ratiometric FRET images (R/G ratio, pseudo-colored as indicated by the color scale, **c**) and normalized FRET efficiency of central (blue line) and peripheral (red line) regions of the synapse (**d**) obtained with TRIRF microscopy of a live Jurkat cell expressing MCS$^+$ during TCR activation. (**e**) Ratiometric FRET images (R/G ratio, pseudo-colored as indicated by the color scale) of MCS$^+$, MCS Lck only and MCS Hras FI and intensity TIRFM images of R-pre GFP, Lact-C2 GFP and Akt PH GFP sensors in Jurkat cells on activating surfaces. (**f**,**g**) FRET efficiency (R/G ratio) of MCS$^+$, MCS Src (containing a different hydrophobic membrane attachment unit as shown in **Fig. 1c**), MCS Lck only and MCS Hras FI (**f**) and intensity of R-pre GFP, Lact-C2 GFP and Akt PH sensors (**g**) at the center (blue) and periphery (red) of immunological synapses. Each symbol represents a single cell measurement of $n \geq 20$ cells for each condition. ns, not significant ($P > 0.05$); $**P < 0.01$ (two-sample tailed t test). Note, data in **g** cannot be statistically compared, as intensity was not normalized to total membrane. Scale bars represent 5 µm (**a**,**c**,**e**) and images are representatives of $n = 5$, 7 and 20 independent experiments, respectively.

the immunological synapse with both fluorescence-lifetime imaging microscopy (FLIM; **Fig. 5a**,**b**) and ratiometric FRET imaging (**Fig. 5c**,**d**). Both regions of the synapse were remodeled during TCR activation (**Fig. 5c**,**d**), with the central part of the synapse exhibiting a greater loss in electrostatic interactions with the membrane, possibly as a result of the greater loss of negatively charged phospholipids or enhanced salt screening. These differences could be quantified, with MCS$^+$ reporting a 8.6 ± 1.0% difference in mean electrostatic potential at central versus peripheral synapse (**Fig. 5e**,**f**). To confirm that the nature of the hydrophobic arms did not influence electrostatic potential measurements, we repeated the experiments using MCS Src (**Fig. 1c**) and measured a similar change in membrane potential (6.0 ± 1.0%.). As expected, MCS Lck only and MCS Hras FI exhibited no differences in FRET efficiencies between the center and periphery of the synapse (**Fig. 5f**). In contrast with MCS$^+$, differences in membrane charges were difficult to visualize with R-pre (**Fig. 5e**) and quantification across the synapse were not straightforward (**Fig. 5g**). It was noteworthy the Lact-C2 and Akt PH sensors reported an accumulation of PS in the central region and phosphatidylinositol (3,4,5)-trisphosphate (PIP_3) in the periphery of the synapse, respectively. This highlights the need for a sensor that reports overall membrane charges and is permanently attached to the membrane, as the distribution of charged lipids may not reflect the local electrostatic potential.

Finally, to evaluate the functional importance of the electrostatic potential on TCR signaling, we manipulated the membrane charge through incorporation of DOTAP (**Fig. 6**). As anticipated, DOTAP lowered the overall capacity for electrostatic interactions with the

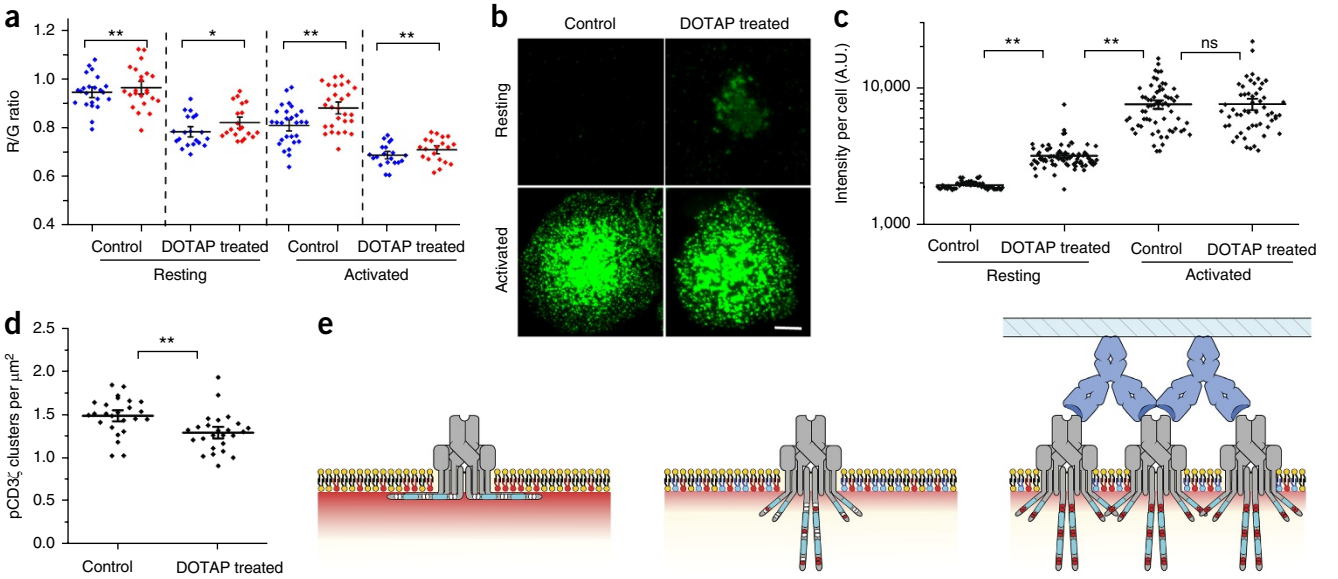

Figure 6 The electrostatic potential of the inner plasma membrane regulates TCR signaling. (**a**) Incorporation of DOTAP lowered FRET efficiency (R/G ratio) of MCS$^+$ in Jurkat cells on resting (poly-L-lysine-coated coverslips) and activating surfaces (coverslips coated with anti-CD3 and anti-CD28 antibodies), but maintained a difference in electrostatic potential between the center (blue) and periphery (red) of the synapse. Controls were cells treated with lipid fusion vesicles that were not enriched in DOTAP. (**b**–**d**) Images (**b**), average intensity per cell (**c**) and number of clusters per μm^2 (**d**) of control and DOTAP-enriched Jurkat cells immunostained for phosphorylated CD3ζ (pCD3ζ) exposed for 5 min to non-activating (resting) and activating surfaces. In **a**, **c** and **d**, each symbols represent a measurement in a single cell of $n \geq 25$ cells per condition. ns, not significance ($P > 0.05$); $^*P < 0.05$, $^{**}P < 0.01$ (paired, two-tailed *t* test assuming equal variance in **a** and **d**, one-way ANOVA with Bonferroni *post hoc* test in **c**). (**e**) Model of TCR signaling. Left, charge interactions between positively charge (light blue) residues in the cytoplasmic tails of the TCR-CD3 complex (gray) and negatively charged (light red) lipids the inner leaflet of the plasma membrane prevent spontaneous phosphorylation of the TCR. Middle, neutralization of the electrostatic potential of the inner plasma membrane (red shading) either by positively charged (light blue) lipids or elevated ion concentration in solution causes the dissociation of cytoplasmic tails from the plasma membrane and spontaneous phosphorylation of tyrosine residues (dark red) in the TCR-CD3 complex. Right, complete TCR-CD3 phosphorylation and TCR clustering requires receptor ligation. Thus, membrane organization including the differences in electrostatic potential across the immunological synapse contributes to TCR clustering and signaling.

membrane, but retained the differences between the central and peripheral part of the plasma membrane (**Fig. 6a**). When we immuno-stained for phosphorylated CD3ζ (pCD3ζ), we observed diffuse pCD3ζ staining in the synapse of non-activated, DOTAP-enriched T cells compared with non-activated control cells (**Fig. 6b**,**c**), strongly suggesting that the reduction in electrostatic interactions with the membrane led to spontaneous TCR phosphorylation. On activating surfaces, we found the anticipated TCR microclusters in activated T cells that accumulated in the center of the synapse (**Fig. 6b**) where electrostatic interactions with the membrane were lower (**Fig. 5f**). We confirmed that expression of the sensor did not limit CD3ζ phosphorylation (**Supplementary Fig. 15f**), allowing the two data sets to be directly compared. Notably, spontaneous CD3ζ phosphorylation on non-activating surfaces, facilitated by DOTAP enrichment, was not sufficient for the formation of TCR clusters in which signaling propagates to drive T cell activation[24,25]. By contrast, in activated DOTAP-enriched T cells, the number of signaling TCR microclusters was significantly reduced compared with control cells ($P < 0.01$; **Fig. 6d**), further indicating that membrane charges not only prevent spontaneous TCR phosphorylation, but may also aid the spatial reorganization of T cell signaling processes following receptor engagement. On the basis of these results, we suggest a model (**Fig. 6e**) in which electrostatic association with the inner leaflet prevents spontaneous and inopportune phosphorylation of the TCR-CD3 complex; a decrease in local electrostatic potential leads to modest levels of TCR phosphorylation; and full activation requires TCR clustering that is facilitated by receptor ligation and membrane organization[11,23,26], including the distribution of the electrostatic potential across the immunological synapse.

DISCUSSION

Recent advances in imaging have revealed a mosaic-like organization of the plasma membrane, with a range of compositionally and functionally distinct membrane domains[27–30]. Although it is generally accepted that membrane charges contribute to the reversible association of proteins with cellular membranes, the extent to which charged membrane domains exist in different cellular membranes and regulate cellular processes such as signaling is less well understood. For example, PS-enriched domains have been identified in the plasma membrane[31], the trans-Golgi network and endocytic organelles[32]. In large organelles such as phagosomes, it is possible to link the remodeling of membrane charges and PS content with protein association and signaling activity[2,33]. However, in the crowded environment of immunological synapses, for example, it is more difficult to identify charged domains and measure their effect on signaling proteins, particularly given that membranes are extensively remodeled during T cell activation[11,23,26].

We developed a FRET-based membrane charge sensor that responds linearly to changes in the negative electrostatic potential of the cytoplasmic leaflet of the plasma membrane, processes fast and reversible kinetics, and is stably associated with cellular membrane. Thus, this sensor is suitable for monitoring dynamic and heterogeneous remodeling processes between and in membranes in live cells. We used our sensor to quantify the effective electrostatic potential under conditions of calcium influx, hypo- and hypertonic treatments, redistribution of PS, and changes in PI phosphorylation, and detected distinct charged membrane domains in the immunological synapse. Thus, the sensor can be employed to assess how membrane channels

and pumps maintain the electrostatic potential, which lipids and proteins result in a permanent alteration in the electrostatic potential or how charged membranes regulate signaling processes.

When applied to T cells, MCS$^+$ revealed a more complex picture of electrostatic membrane interactions in the immunological synapse[11], where the distribution of charged lipids did not necessarily reflect the effective electrostatic potential and the membrane association of the cytosolic tails of the TCR-CD3 complex. For example, the negative electrostatic potential was higher in the periphery of the synapse, where PIP3 is found at high concentrations[34], but was lower in the center, where PS seemed to accumulate (**Fig. 5**) and where TCR signaling clusters reside in activated T cells[35]. Thus, PS levels are unlikely to reflect the extent of the electrostatic membrane interactions of the TCR-CD3 complex, as previously suggested[36]. Indeed, directly manipulating the electrostatic potential with an inert cationic lipid (**Fig. 6**) revealed that neutralization of charge, rather than reorganization of phospholipids in the synapse, is responsible for the change in electrostatic potential. One well-characterized mechanism of PS charge neutralization is increased cytoplasmic Ca^{2+} concentration, which results in dissociation of CD3ε cytoplasmic tails from the membrane and enhanced phosphorylation[22]. Whether Ca^{2+} concentrations are elevated locally or globally during T cell activation, and initiate or amplify TCR signaling, remains unknown.

In conclusion, our sensors are ideally suited for more nuanced investigations of spatial and temporal changes in membrane potential, the mechanisms that control these, and the effect these changes have on cellular processes.

METHODS

Methods, including statements of data availability and any associated accession codes and references, are available in the online version of the paper.

ACKNOWLEDGMENTS

We acknowledge technical assistant by the BioMedical Imaging Facility, University of New South Wales. K.G. and J.R. acknowledge funding from the ARC Centre of Excellence in Advanced Molecular Imaging (CE140100011 to K.G.) and National Health and Medical Research Council of Australia (1059278 and 1037320 to K.G., 1022182 to K.G. and J.R.). J.J.G. acknowledges funding from the ARC Centre of Excellence in Convergent Bio-Nano Science and Technology (CE140100036) the Australian Research Council for an Australian Laureate Fellowship (FL150100060) and a National Health and Medical Research Council of Australia program grant (1091261).

AUTHOR CONTRIBUTIONS

Y.M. performed experiments, analyzed data and wrote the manuscript.
Y.Y. performed and analyzed experiments. P.R.N. established and performed analysis. J.G. and J.R. contributed to data interpretation and manuscript writing. J.J.G. contributed to data analysis and interpretation and manuscript writing. K.G. designed the project and wrote the manuscript.

COMPETING FINANCIAL INTERESTS

The authors declare no competing financial interests.

1. McLaughlin, S., Smith, S.O., Hayman, M.J. & Murray, D. An electrostatic engine model for autoinhibition and activation of the epidermal growth factor receptor (EGFR/ErbB) family. *J. Gen. Physiol.* **126**, 41–53 (2005).
2. Yeung, T. *et al.* Receptor activation alters inner surface potential during phagocytosis. *Science* **313**, 347–351 (2006).
3. Yeung, T. & Grinstein, S. Lipid signaling and the modulation of surface charge during phagocytosis. *Immunol. Rev.* **219**, 17–36 (2007).
4. Lomize, A.L., Pogozheva, I.D., Lomize, M.A. & Mosberg, H.I. The role of hydrophobic interactions in positioning of peripheral proteins in membranes. *BMC Struct. Biol.* **7**, 44 (2007).
5. McLaughlin, S. & Aderem, A. The myristoyl-electrostatic switch: a modulator of reversible protein-membrane interactions. *Trends Biochem. Sci.* **20**, 272–276 (1995).
6. van den Bogaart, G. *et al.* Membrane protein sequestering by ionic protein-lipid interactions. *Nature* **479**, 552–555 (2011).
7. Alexander, R.T. *et al.* Membrane surface charge dictates the structure and function of the epithelial Na^+/H^+ exchanger. *EMBO J.* **30**, 679–691 (2011).
8. McLaughlin, S. The electrostatic properties of membranes. *Annu. Rev. Biophys. Biophys. Chem.* **18**, 113–136 (1989).
9. Ohki, S. Membrane potential, surface potential and ionic permeability. *Phys. Lett. A* **75**, 149–152 (1979).
10. Okeley, N.M. & Gelb, M.H. A designed probe for acidic phospholipids reveals the unique enriched anionic character of the cytosolic face of the mammalian plasma membrane. *J. Biol. Chem.* **279**, 21833–21840 (2004).
11. Gagnon, E., Schubert, D.A., Gordo, S., Chu, H.H. & Wucherpfennig, K.W. Local changes in lipid environment of TCR microclusters regulate membrane binding by the CD3ε cytoplasmic domain. *J. Exp. Med.* **209**, 2423–2439 (2012).
12. Yeung, T. *et al.* Membrane phosphatidylserine regulates surface charge and protein localization. *Science* **319**, 210–213 (2008).
13. Ben-Tal, N., Honig, B., Peitzsch, R.M., Denisov, G. & McLaughlin, S. Binding of small basic peptides to membranes containing acidic lipids: theoretical models and experimental results. *Biophys. J.* **71**, 561–575 (1996).
14. Cohen, J.A. & Cohen, M. Adsorption of monovalent and divalent cations by phospholipid membranes. The monomer-dimer problem. *Biophys. J.* **36**, 623–651 (1981).
15. Harb, F.F. & Tinland, B. Effect of ionic strength on dynamics of supported phosphatidylcholine lipid bilayer revealed by FRAPP and Langmuir-Blodgett transfer ratios. *Langmuir* **29**, 5540–5546 (2013).
16. Perez, J.B., Martinez, K.L., Segura, J.M. & Vogel, H. Supported cell-membrane sheets for functional fluorescence imaging of membrane proteins. *Adv. Funct. Mater.* **16**, 306–312 (2006).
17. Denis, V. & Cyert, M.S. Internal Ca^{2+} release in yeast is triggered by hypertonic shock and mediated by a TRP channel homologue. *J. Cell Biol.* **156**, 29–34 (2002).
18. Koldenkova, V.P., Matsuda, T. & Nagai, T. MagIC, a genetically encoded fluorescent indicator for monitoring cellular Mg^{2+} using a non-Förster resonance energy transfer ratiometric imaging approach. *J. Biomed. Opt.* **20**, 101203 (2015).
19. Zhang, H., Cordoba, S.-P., Dushek, O. & van der Merwe, P.A. Basic residues in the T-cell receptor ζ cytoplasmic domain mediate membrane association and modulate signaling. *Proc. Natl. Acad. Sci. USA* **108**, 19323–19328 (2011).
20. Xu, C. *et al.* Regulation of T cell receptor activation by dynamic membrane binding of the CD3epsilon cytoplasmic tyrosine-based motif. *Cell* **135**, 702–713 (2008).
21. Bettini, M.L. *et al.* Membrane association of the CD3ε signaling domain is required for optimal T cell development and function. *J. Immunol.* **193**, 258–267 (2014).
22. Shi, X. *et al.* Ca^{2+} regulates T-cell receptor activation by modulating the charge property of lipids. *Nature* **493**, 111–115 (2013).
23. Zech, T. *et al.* Accumulation of raft lipids in T-cell plasma membrane domains engaged in TCR signaling. *EMBO J.* **28**, 466–476 (2009).
24. Yokosuka, T. *et al.* Newly generated T cell receptor microclusters initiate and sustain T cell activation by recruitment of Zap70 and SLP-76. *Nat. Immunol.* **6**, 1253–1262 (2005).
25. Pageon, S.V . *et al.* Functional role of T-cell receptor nanoclusters in signal initiation and antigen discrimination. *Proc. Natl. Acad. Sci. USA* **113**, E5454–E5463 (2016).
26. Gaus, K., Chklovskaia, E., Fazekas de St Groth, B., Jessup, W. & Harder, T. Condensation of the plasma membrane at the site of T lymphocyte activation. *J. Cell Biol.* **171**, 121–131 (2005).
27. Murase, K. *et al.* Ultrafine membrane compartments for molecular diffusion as revealed by single molecule techniques. *Biophys. J.* **86**, 4075–4093 (2004).
28. Goswami, D. *et al.* Nanoclusters of GPI-anchored proteins are formed by cortical actin-driven activity. *Cell* **135**, 1085–1097 (2008).
29. Gowrishankar, K. *et al.* Active remodeling of cortical actin regulates spatiotemporal organization of cell surface molecules. *Cell* **149**, 1353–1367 (2012).
30. Eggeling, C. *et al.* Direct observation of the nanoscale dynamics of membrane lipids in a living cell. *Nature* **457**, 1159–1162 (2009).
31. Zhou, Y. *et al.* Membrane potential modulates plasma membrane phospholipid dynamics and K-Ras signaling. *Science* **349**, 873–876 (2015).
32. Fairn, G.D. *et al.* High-resolution mapping reveals topologically distinct cellular pools of phosphatidylserine. *J. Cell Biol.* **194**, 257–275 (2011).
33. Yeung, T. *et al.* Contribution of phosphatidylserine to membrane surface charge and protein targeting during phagosome maturation. *J. Cell Biol.* **185**, 917–928 (2009).
34. Le Floc'h, A. *et al.* Annular PIP3 accumulation controls actin architecture and modulates cytotoxicity at the immunological synapse. *J. Exp. Med.* **210**, 2721–2737 (2013).
35. Rossy, J., Owen, D.M., Williamson, D.J., Yang, Z. & Gaus, K. Conformational states of the kinase Lck regulate clustering in early T cell signaling. *Nat. Immunol.* **14**, 82–89 (2013).
36. Hui, E. & Vale, R.D. *In vitro* membrane reconstitution of the T-cell receptor proximal signaling network. *Nat. Struct. Mol. Biol.* **21**, 133–142 (2014).

ONLINE METHODS

General methods and materials All DNA oligonucleotides were purchased from Sigma-Aldrich Australia. The original R-pre construct was kindly provided by Sergio Grinstein (University of Toronto). Primer sequences are listed in **Supplementary Table 1**. *Phusion* DNA polymerase (New England BioLabs) was used for all PCR reactions. Subcloning was conducted by either restriction enzyme digestion (New England BioLabs) or overlapping extension. Plasmid sequences were confirmed by BigDye Terminator v3.1 Cycle Sequencing (Life Technologies) at the Ramaciotti Centre for Genomics at the University of New South Wales.

Plasmids. The EGFPN1 vector (Clontech) was used as vector backbone all plasmids. The membrane localization motif of the tyrosine kinase Lck (MGCIKSKRKDNLNDDGVDMKT) was added to the N terminus of EGFP, with a linker sequence of GGGGDP. The charge sensitive membrane-binding motif of R-pre (ARDGRRRRRRARARCVIM) was added to the C terminus of mCherry inserted at the C terminus of EGFP. Between the two fluorescent proteins a linker with the sequence of RRRRSG was added (**Supplementary Fig. 1a**,**b**). For the construct MCS 0.2 and onwards, the linker was reduced to SG. For MCS 0.3 and onwards, EGFP was replaced with Venus and a section of the C terminus of Venus (GITLGMDELYK) and the C terminus of mCherry (DELYK) were deleted to increase FRET efficiency (**Supplementary Fig. 1c**). The MCS vector was used for the construction of the control constructs. In MCS Lck only and MCS R-pre only constructs, the Lck10 or R-pre sequences were deleted, respectively. In MCS Src, Lck10 was replaced by the membrane anchor of Src (Src15). In MCS Hras and MCS Hras FI (**Fig. 1c**), the R-pre sequence of MCS was replaced by the C terminus of Hras or modified Hras sequence. The sequences are listed in **Supplementary Table 1.**

Optimization of the FRET sensor. We enhanced the maximum FRET efficiency of the sensor under conditions of high negative membrane potential by changing the length of the linker between the two fluorescent proteins (**Supplementary Fig. 1**). In the final version, 11 amino acids from the C terminus of Venus and 7 amino acids from the N terminus of mCherry were removed. Only two amino acids (serine and glycine) were needed to allow the free rotation of the acceptor, and thus a concomitant reduction in FRET, when the membrane negative charge was lowered and the MA2 detached from the plasma membrane (**Supplementary Fig. 1a–c**). This is consistent with previous reports suggesting that rotation between FRET pairs alters FRET efficiency even in tandem dimers[37,38]. Furthermore, the distance of the sensor to the membrane was minimized by limiting the first membrane attachment unit to 10 amino acids (Lck10) and removing 5 amino acids from C terminus of mCherry (**Supplementary Fig. 1a**).

We noticed, however, that some of the earlier versions of the sensors (for example MSC 0.4) detached from the membrane (**Supplementary Figs. 1d**,**e** and **2**). This finding is counter-intuitive as one would expect that the farnesylation group in R-pre would anchor the protein to the membrane. However, the maturation rate of lipid modifications can vary and is difficult to control. Thus, we mutated the farnesylated cysteine in the ARCVIM motif at the C terminus in MA2. This version (MCS 0.5) and subsequent version of the sensor remained attached to the plasma membrane, even at low negative electrostatic potentials (MCS 0.5, **Supplementary Fig. 1f**,**g**). Finally, we tuned the binding efficiency of the electrostatic anchor to the inner leaflet of the plasma membrane by replacing the cysteine and alanine residues in the ARCVIM motif with tryptophan and phenylalanine (MCS; **Fig. 1c**) and further replacing aspartic acid and alanine residues in the RDGRRRRRAR motif with phenylalanine and isoleucine residues, respectively (MCS$^+$; **Fig. 1c**). In addition, we engineered controls constructs where the charge-sensitive arm MA2 was replaced with the hydrophobic membrane attachment motif of H-Ras (MCS Hras; **Fig. 1c**). This anchor was largely charge insensitive when truncated so that the RKLNPPDE sequence was removed and the serine and proline residues in the remaining sequence mutated to phenylalanine and isoleucine residues, respectively (MCS Hras FI; **Fig. 1c**,**d**). Thus even naturally occurring hydrophobic membrane attachment motifs contain some electrostatic interaction.

Cell culture and transfection. COS-7 (ATCC CRL-1651) and HeLa (ATCC CCL-2) cells were cultured in Dulbecco's Modified Eagle's medium (DMEM) supplemented with 10% fetal bovine serum (FBS). Jurkat E6-1 (ATCC TIB-152) cells were cultured in Roswell Park Memorial Institute medium (RPMI) supplemented with 10% FBS. All cells were cultured in 37 °C incubators with 5% CO_2. For transfection of adherent cells, 18 h before transfection, cells were trypsinized and plated in glass bottom Fluorodish cell culture dishes (Coherent Scientific) of 35-mm diameter. Cell transfection was conducted using Lipofectamine LTX (Invitrogen). Jurkat E6-1 cells were transfected using an electroporator (Invitrogen Neon) following the manufacturer's protocols. All cells were imaged 18–24 h post transfection. All cell lines were tested and confirmed to be *Mycoplasma* negative. Jurkat cells were tested by anti-CD3 antibody-induced Ca^{2+} influx and CD69 upregulation.

Cell treatment and imaging conditions. Membrane sheets were generated as previously described[16]. Briefly, the cell medium was exchanged to 10 mM Ca^{2+}- and Mg^{2+}-free phosphate buffered saline (PBS) for 30 s. Cells swelled under these conditions due to low cytosolic osmotic pressure. A poly-L-lysine (PLL)-coated coverslip, glued to the opening of a 1.5-ml microcentrifuge tube, was placed on top of the cells, and gentle pressure was applied to ensure that the PLL-coated coverslip made contact with the cell membrane. After 2 min, the microcentrifuge tube with the PLL-coated coverslip was quickly removed, which produced a 'pop' sound. This procedure resulted in the apical section of the plasma membrane being removed while the basolateral section of the membrane remained attached to the substratum. The membrane sheet was washed gently three times in 10 mM Ca^{2+}- and Mg^{2+}-free PBS before the ionic strength titration treatments.

For ionic strength titration experiments, appropriate and discrete volumes of 1.5 M Ca^{2+}- and Mg^{2+}-free PBS was added to the initial 10 mM solution, followed by a mixing of the solution by pipetting and a 2-min incubation period. For the fast disassociation and association kinetics experiments, the ionic strength was rapidly changed from 10 mM to 275 mM, or from 275 mM to 35 mM. The former was done by adding ten volumes of 300 mM NaCl solution to one volume of 10 mM NaCl solution. The latter was achieved by adding ten volumes of 10 mM NaCl to one volume of 275 mM NaCl.

For the lipid fusion experiments, Fuse-it-L (Ibidi) lipid vesicles were loaded with lipid and fused with cell membranes according to the manufacture's protocol. The lipid vesicles were composed of mixture of 1,2-dioleoyl-sn-glycero-3-phosphoethanolamine 18:1 (Δ9-Cis DOPE), 1,2-dioleoyl-3-trimethylammonium-propane 18:1 (DOTAP), and 1,1′-dioctadecyl-3,3,3′,3′-tetramethylindotricarbocyanine iodide DiR at 1:1:0.05 w/w ratio. 1,2-dioleoyl-sn-glycero-3-phospho-L-serine 18:1 (PS) and DOTAP were mixed with Fuse-it-L vesicle at molar concentration ratios of 2:3. The lipid mixture was dried under nitrogen gas and rehydrated in 10 mM PBS for fusion with membrane lawns or in HBSS Ca^{2+}-containing buffer (1.3 mM $CaCl_2$, 0.5 mM $MgCl_2$, 0.4 mM $MgSO_4$, 5.3 mM KCl, 0.4 mM KH_2PO_4, 4.2 mM $NaHCO_3$, 127 mM NaCl, 0.3 mM Na_2HPO_4) for fusion with T cells. The lipids were diluted 50 times and sonicated for 25 min before incubation with membrane lawns or cells at 1:2 v/v ratios.

For the Ca^{2+} influx experiment, ionomycin (Sigma-Aldrich) or thapsigargin (Sigma-Aldrich) was added to the cell medium at a final concentration of 10 μM or 40 μM, respectively. The medium contained 25 mM HEPES, 80 mM NaCl, 5 mM KCl, 44 mM $NaHCO_3$, 2 mM $CaCl_2$, 1 mM $MgSO_4$, 25 mM Glucose. For thapsigargin treatment, additional 5 mM of $CaCl_2$ was introduced to the medium. In the PS flipping and translocation experiments, dibucaine (Sigma-Aldrich) or Fendiline (Cayman Chemical) were added to Ca^{2+}-free medium at a final concentration of 1 mM and 60 μM, respectively. Time-lapse imaging was started 30 s before the addition of drugs and images acquired at 0.5–5.0 Hz.

Jurkat E6.1 cells were either activated by antibody-coated beads or antibody-coated coverslips. For activation with antibody-coated beads, anti-human CD3ε (OKT3, eBioscience #16-0037-85) and anti-human CD28 (CD28.2, eBioscience #16-0037-85) antibodies were first conjugated to 3.5-μm diameter streptavidin-coated polystyrene beads (Spherotech). Jurkat cells were mixed with the antibody-coated beads and activated at 37° for 10 min. Cells were fixed by 4% paraformaldehyde and mounted (Dako Agilent Technology) to coverslip for imaging. For activation with antibody-coated surfaces, the same anti-human CD3ε and anti-human CD28 antibodies were used. For immunostaining in **Figure 6**, a primary antibody against CD3ζ Y142 that directly conjugated with Alexa Fluo647 (K25-407.69, BD Biosciences #558489) was used. All antibodies were validated by the manufacturer.

Microscopy. All confocal imaging experiments were performed on a Leica TCS SP5 microscope. Prior to imaging, the cell medium was changed to HEPES-buffered medium with no phenol red. A 63× objective lens (NA = 1.4, oil immersion) was used for all image acquisition. For standard, high-resolution image acquisition, the galvo-scanner was used. The pinhole size was set to one airy unit. Typically, 16 lines were averaged to increase the signal-to-noise ratio. For K_{on} and K_{off} measurements, the 8,000-Hz resonance scanner was used. Under bidirectional scanning mode, the frame rate was increased to 100 Hz at 64 × 64 image size. To acquire sufficient signal, the pinhole was set to two airy units. For FRET imaging, a 488-nm argon ion laser was used for excitation, and the fluorescence emission was split into two spectral emission regions, 505–555 nm and 610–700 nm, to simultaneously collect donor and acceptor emission. The laser intensity and detector were adjusted so that no pixel saturation occurred throughout the acquisition. For *x-z* imaging, a line was chosen in the center of the cell, and the laser was scanned along the line at increasing depth. For spectral imaging, the probe was excited with a 458-nm argon ion laser, and the fluorescence spectrum was collected from 480–700 nm by moving the emission monochrometer with 3-nm step size and 5-nm slit width.

T cell activation under total internal reflection fluorescence (TIRF) illumination was imaged with a Zeiss Elyra PS.1 microscope. A 488-nm argon ion laser was used for excitation through a Zeiss 100× (NA = 1.57) oil objective. The emitted fluorescence was separated from the excitation (beamsplitter LBF 488/561) and separated by band pass filters into two regions, 495–550 nm and 570–620 nm, that were collected by two cooled EMCCD cameras (Andor Ixon 897). The camera alignment was achieved by the Zeiss Duolink system. The frame rate for image acquisition was set to 500 ms. Image format was 512 pixels × 512 pixels with pixel size of 100 nm.

FLIM imaging was performed on a Leica TCS SP5 microscope coupled to a Microtime 200 system (PicoQuant). Time-correlated single photon counting (TCSPC) was used for fluorescence lifetime measurement. A 80-MHz pulsed locked-in titanium-sapphire laser was tuned to 900 nm and used as the excitation laser. The emitted fluorescence was coupled into an optical fiber at the external X1 port after passing a 700-nm short pass filter. The fiber was attached to the import port of MicroTime 200 main optical unit. The donor and acceptor fluorescence was separated onto two SPAD detectors (PDM, MPD and tau-SPAD, PicoQuant) by a 555-nm beam splitter, and further filtered by 525/50-nm and 617/73-nm band pass filters (Semrock), respectively. Data were acquired in time-tagged time-resolved mode (TTTR) mode by a PicoHarp 300 (PicoQuant) photon-counting unit, using a reference diode signal from the pulsed Ti:Sapphire laser. FLIM image reconstruction and lifetime analysis was performed by following the previous method[39] using custom-written software (TTTR Data Analysis, developed in LabVIEW). To collect sufficient numbers of photons for the lifetime histogram reconstruction at each pixel, the line accumulation was used to reach an accumulated pixel dwell time of 2 ms. The time delay between the photon arrival time and the excitation pulse, which is used for the TCSPC histogram reconstruction, was encoded in the TTTR file.

Image analysis. Comparison of intensity and FRET signals between cell regions was performed with a semi-automated MATLAB GUI. Single- or dual-channel CZI (Zeiss Microscopy) or TIFF images were loaded into the GUI. A user-defined intensity threshold used to segment the cell region from the background. This thresholded mask was eroded by a user-defined distance (30 pixels for center versus periphery detection at TIRF images of T cell synapse in **Fig. 5**; 10 pixels for the plasma membrane *versus* cytoplasm comparison for intensity-based sensors in **Fig. 5** and **Supplementary Fig. 14**). The portion of the thresholded mask remaining after erosion was taken as the synapse or cell center. The portion removed by erosion, determined by taking the difference between the original thresholded mask and the eroded mask, was taken as the synapse or cell periphery. Pixel intensities falling in each of these masks in the intensity images were used to determine either mean intensity or, with pixel-wise analysis followed by averaging, mean FRET ratios in each region.

To plot the change in FRET efficiency over time, either as a plot of R/G values for single cell as a function of time, for example, **Figure 1d**, or before and after drug treatment of a cell population, for example, **Figure 3d**, the data were normalized to the initial R/G value before the treatment. For the comparison of FRET efficiencies between different versions of the sensors, for example, **Figure 1**, or among different regions of the cell for example, **Figure 5f**, the raw R/G ratio values were used. The FRET kymograph in **Figure 3c** was acquired by plotting the R/G line profile in the selected line as a function of time.

Model fitting and statistical analysis. Curve plotting, model fitting and related statistical analysis of the ionic strength titration and kinetics analysis were done in OriginPro (OriginLab) and Prism (GraphPad). The MCS k_{off} rate was quantified as the residence time, which was the time required for the sensor to lose 50% of its initial FRET signal when the ionic strength was increased suddenly from 10 mM to 275 mM. The k_{on} rate was extracted by fitting the R/G curve to first order integrated rate equation $A = A_0{}^*\exp(-kt)$ as the ionic strength was exchanged from 275 mM to 35 mM. In order to see how the FRET signal is related to the membrane charge potentials, the FRET curve from the equilibrium titration experiment was fitted to Debye-Hückel models. Here, the Debye length directly represents the membrane electric charge potential or zeta potential.

$$k^{-1} = \sqrt{\varepsilon_0 \varepsilon_\Upsilon K_B T / 2 N_A e^2 I}$$

where κ^{-1} is the Debye length in electrolyte solution; ε_0 the permittivity of free space ($8.85419{}^*10^{12} A^2 S^4\ kg^{-1} m^{-3}$); ε_Υ the dielectric constant (80); K_B is the Boltzmann's constant; T the absolute temperature (298 K); NA the Avogadro number; e represents an elementary charge and I the ionic strength (in M)[40]. For the extended Debye-Hückel model, where the activity coefficient of the ions was considered, the membrane charge potential can be described by

$$k^{-1} = \sqrt{\varepsilon_0 \varepsilon_\Upsilon K_B T / 2 N_A e^2 a I}$$

a is the activity coefficient of the major ions in solution, in the case of NaCl,

$$a = 10^{\frac{-(0.5 * \sqrt{I})}{(1 + 0.98 * \sqrt{I})}}$$

and I is the ionic strength of the solution. To facilitate the fitting, a shifting and scaling factor, M and N, was incorporated into the equation, as

$$k^{-1} = \mathrm{M} + \mathrm{N} * \sqrt{\varepsilon_0 \varepsilon_\Upsilon K_B T \Big/ 2 N_A e^2\, 10^{\frac{-(0.5\sqrt{I})}{(1 + 0.98 * \sqrt{I}) I}}}$$

The fitting procedure was conducted in OriginPro using the Levenberg-Marquardt algorithm. The adjusted R^2 value was used as an indication of the goodness of the fitting.

The lifetime analysis was also performed with the custom written software (TTTR Data Analysis, developed in LabVIEW). To compare the donor lifetime at the center and periphery of the synapse (**Fig. 5a**), region specific mask files of the desired membrane regions were extracted and analyzed separately using the Labview program. The average photon arrival times in the selected region were taken as the average donor lifetime, which was compared by paired *t* test.

For statistical analysis between two samples, either two-sample two-tailed *t* test assuming equal variance (that is, for comparisons between cells) or paired *t*-test assuming equal variance (that is, for comparisons of regions within the same cell) were used. For comparison of multiple samples, one-way ANOVA with a post hoc Bonferroni test was used. In box plots, the mean and s.e. were provided with the standard error calculated as SD/√n.

Data availability. Data available upon request to the corresponding author. Code for the MATLAB GUI is freely available from the authors' Git repository at https://github.com/PRNicovich/NBT-RA37689.git.

37. Meng, F., Suchyna, T.M. & Sachs, F. A fluorescence energy transfer-based mechanical stress sensor for specific proteins in situ. *FEBS J.* **275**, 3072–3087 (2008).
38. Meng, F. & Sachs, F. Orientation-based FRET sensor for real-time imaging of cellular forces. *J. Cell Sci.* **125**, 743–750 (2012).
39. Benda, A., Ma, Y. & Gaus, K. Self-calibrated line-scan STED-FCS to quantify lipid dynamics in model and cell membranes. *Biophys. J.* **108**, 596–609 (2015).
40. Lloret, N. *et al.* Effects of buffer composition and dilution on nanowire field-effect biosensors. *Nanotechnology* **24**, 035501 (2013).

doi:10.1038/nbt.3828

Addendum

Editorial Expression of Concern: DNA-guided genome editing using the *Natronobacterium gregoryi* Argonaute

Feng Gao, Xiao Z Shen, Feng Jiang, Yongqiang Wu & Chunyu Han
***Nat. Biotechnol.* 34, 768–773 (2016); published online 2 May 2016; addendum published after print 28 November 2016**

The editors of *Nature Biotechnology* are issuing an editorial expression of concern regarding this article to alert our readers to concerns regarding the reproducibility of the original results. At this time, we are publishing the results of three groups (http://dx.doi.org/10.1038/nbt.3753) that have tried to reproduce the results in the critical Figure 4 in the original paper by Han and colleagues, which demonstrates editing of endogenous genomic loci in mammalian cells. None of the groups observed any induction of mutations by NgAgo at any of the loci or under any of the conditions tested above the sensitivity of the assays used. Similar results have been recently reported by a different group of authors in *Protein & Cell* (doi:10.1007/s13238-016-0343-9).

We are in contact with the authors, who are investigating potential causes for the lack of reproducibility. The authors have been informed of this statement. While the investigations are ongoing, Chunyu Han and Xiao Z. Shen agree with this editorial expression of concern. Feng Gao, Feng Jiang and Yongqiang Wu do not feel that it is appropriate at this time.

We will update our readers once these investigations are complete.

Erratum: Drugging the gut microbiome

Ken Garber
***Nat. Biotechnol.* 34, 228–231 (2015); published online 6 March 2015; corrected after print 12 October 2016**

In the version of this article initially published, on p.231, left-hand column, the maker of linaclotide was said to be Redwood rather than Ironwood Pharmaceuticals. In addition, linaclotide is no longer referred to as a "homolog of the enterotoxin peptides," but as "similar to the enterotoxin peptides," and it has been clarified to be "rationally designed." The errors have been corrected in the HTML and PDF versions of the article.

Erratum: An optical probe of synaptic plasticity

Tal Laviv & Ryohei Yasuda
***Nat. Biotechnol.* 35, 26–27 (2017); published online 10 January 2017; corrected after print 30 March 2017**

In the version of this article initially published, reference 1 was missing the author's first initial. The error has been corrected in the HTML and PDF versions of the article.

Corrigendum: Response to "Railroading at the FDA"

Francesco Muntoni, Sue Fletcher & Steve Wilton
***Nat. Biotechnol.* 35, 207–209 (2017); published online 7 March 2017; corrected after print 30 March 2017**

In the version of this article initially published, F.M. was credited for giving input on study design and data analysis, which he did not. The error has been corrected in the HTML and PDF versions of the article.

Corrigendum: A FRET sensor enables quantitative measurements of membrane charges in live cells

Yuanqing Ma, Yui Yamamoto, Philip R Nicovich, Jesse Goyette, Jérémie Rossy, J Justin Gooding & Katharina Gaus
***Nat. Biotechnol.* doi:10.1038/nbt.3828; published online 13 March 2017; corrected after print 31 March 2017**

In the version of this article initially published, in the Figure 1 legend, the following text was inserted: "(**d**), and the average FRET efficiencies in transfected COS-7 cells (**e**)"; in Figure 2d, the right-hand *y* axis was given as "PS fusion," rather than "DOTAP fusion"; in text beneath Figure 2, figure callouts were corrected and additional text added as follows: "275 mM (**Fig.1d**,**e**)" should read "275 mM (**Fig. 1d**)", "9 mM (**Fig. 1e**)" should read "9 mM (**Fig. 1f**)", "FI exhibited no" should be "FI exhibited different FRET efficiencies in intact cells (**Fig. 1e**) and no," "strength (**Fig. 1c**–**f**)" should be "strength (**Fig. 1c**,**d**,**f**)," "reach 50% in" should be "reach 50% change in"; in text beneath Figure 3, "MCS^+ (**Fig. 2e**–**g**)" should be "MCS^+ (**Fig. 2e**,**f**)"; in Figure 3 legend, "s.e." should read "s.e.m." The errors have been corrected in the HTML and PDF versions of the article.